Published in final edited form as:

Curr Biol. 2021 February 22; 31(4): 733–741.e7. doi:10.1016/j.cub.2020.11.027.

Orientation Preference Maps in *Microcebus murinus* Reveal Size-Invariant Design Principles in Primate Visual Cortex

Chun Lum Andy Ho[1,11], **Robert Zimmermann**[1,11], **Juan Daniel Flórez Weidinger**[2], **Mario Prsa**[1], **Manuel Schottdorf**[2], **Sam Merlin**[3], **Tsuyoshi Okamoto**[4], **Koji Ikezoe**[5], **Fabien Pifferi**[6], **Fabienne Aujard**[6], **Alessandra Angelucci**[3], **Fred Wolf**[2,7,8,9,10], **Daniel Huber**[1,12,*]

[1]University of Geneva, Department of Basic Neurosciences, Rue Michel Servet 1, Geneva 1211, Switzerland

[2]Max Planck Institute for Dynamics and Self-Organization, Am Faßberg 17, Göttingen 37077, Germany

[3]Moran Eye Center, University of Utah, Department of Ophthalmology and Visual Science, 65 Mario Capecchi Drive, Salt Lake City, UT 84132, USA

[4]Kyushu University, Faculty of Arts and Science, 744 Motooka Nishi-ku, Fukuoka 819-0395, Japan

[5]Center for Information and Neural Networks, Osaka University and National Institute of Information and Communications Technology, Graduate School of Frontier Biosciences, 1-3 Yamadaoka Suita, Osaka 565-0871, Japan

[6]UMR CNRS/MNHN 7179, Mécanismes Adaptatifs et Evolution, 1 Avenue du Petit Chateau, Brunoy 91800, France

[7]Campus Institute for Dynamics of Biological Networks, Hermann-Rein-Straße 3, Göttingen 37075, Germany

[8]Bernstein Center for Computational Neuroscience, Hermann-Rein-Straße 3, Göttingen 37075, Germany

[9]Max Planck Institute of Experimental Medicine, Hermann-Rein-Straße 3, Göttingen 37075, Germany

[10]Institute for Dynamics of Complex Systems, Georg-August University, Friedrich-Hund-Platz 1, Göttingen 37073, Germany

*Correspondence: daniel.huber@unige.ch.

AUTHOR CONTRIBUTIONS

D.H. conceptualized the study. D.H., C.L.A.H., R.Z., and M.P. designed the experiments. C.L.A.H. and R.Z. ran the experiments. F.W. and J.D.F.W. designed models and cross-species comparative analyses. C.L.A.H., J.D.F.W., M.S., and M.P. analyzed the data. F.W. and D.H. oversaw data analysis. S.M., K.I., T.O., and A.A. provided the macaque data. F.P. and F.A. provided expertise, guidance, and resources related to the mouse lemurs. D.H., C.L.A.H., and F.W. wrote the manuscript.

SUPPLEMENTAL INFORMATION

Supplemental Information can be found online at https://doi.org/10.1016/j.cub.2020.11.027.

DECLARATION OF INTERESTS

The authors declare no competing interests.

[11]These authors contributed equally

[12]Lead Contact

SUMMARY

Orientation preference maps (OPMs) are a prominent feature of primary visual cortex (V1) organization in many primates and carnivores. In rodents, neurons are not organized in OPMs but are instead interspersed in a “salt and pepper” fashion, although clusters of orientation-selective neurons have been reported. Does this fundamental difference reflect the existence of a lower size limit for orientation columns (OCs) below which they cannot be scaled down with decreasing V1 size? To address this question, we examined V1 of one of the smallest living primates, the 60-g prosimian mouse lemur (*Microcebus murinus*). Using chronic intrinsic signal imaging, we found that mouse lemur V1 contains robust OCs, which are arranged in a pinwheel-like fashion. OC size in mouse lemurs was found to be only marginally smaller compared to the macaque, suggesting that these circuit elements are nearly incompressible. The spatial arrangement of pinwheels is well described by a common mathematical design of primate V1 circuit organization. In order to accommodate OPMs, we found that the mouse lemur V1 covers one-fifth of the cortical surface, which is one of the largest V1-to-cortex ratios found in primates. These results indicate that the primate-type visual cortical circuit organization is constrained by a size limitation and raises the possibility that its emergence might have evolved by disruptive innovation rather than gradual change.

Graphical Abstract

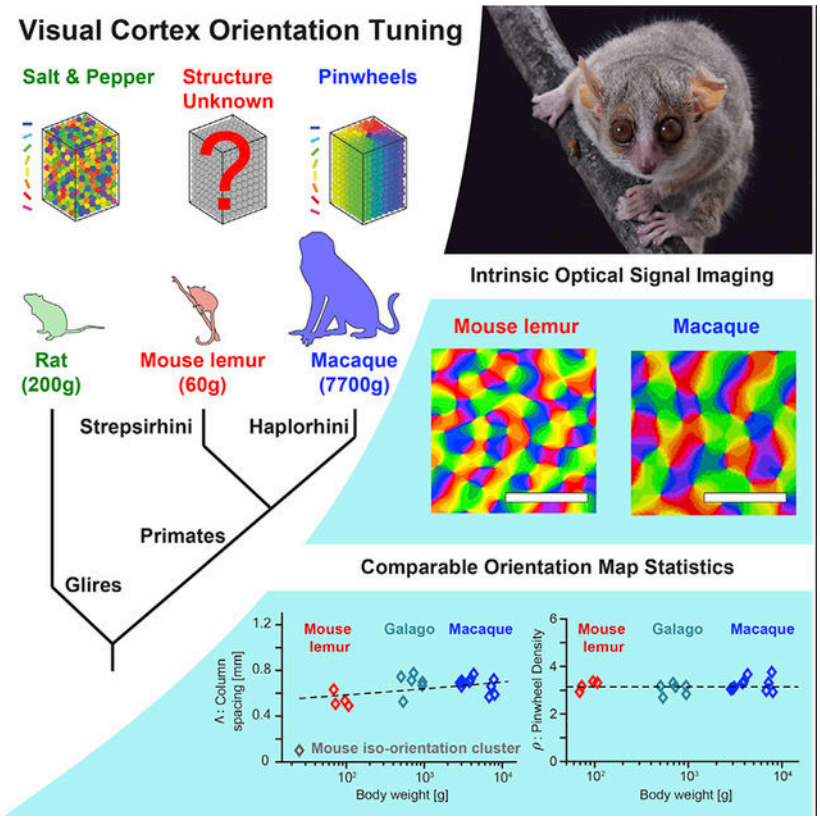

In Brief

Orientation preference maps are a hallmark of V1 organization in all primates studied thus far, yet they are absent in rodents. It is uncertain whether these structures scale with body or brain size. Using intrinsic signal imaging, Ho et al. reveal the presence of such maps in the V1 of the world's smallest primate, the mouse lemur (*Microcebus murinus*).

INTRODUCTION

Primates and rodents are closely related. The two lineages probably evolved from a common ancestor between the late Cretaceous and the early Eocene[1,2] (Figure 1A). In contrast to most rodents, primates developed into highly encephalized and visual animals, which entailed substantial transformations of their cortical visual system.[3] These transformations specifically affected the functional architecture of the primary visual cortex (V1). Orientation-tuned neurons in primate V1 (as well as in carnivores and ungulates) are clustered into functional orientation columns[4–6] and arranged in a pinwheel-like manner. Such an organization can minimize wiring length, economizing the volume, building, and maintenance cost of V1.[7] Adjacent columns with the same preferred orientation exhibit a typical spacing, Λ. A V1 subregion of area of Λ^2, termed hypercolumn area, will typically contain the full set of orientation preferences.[8–10] In contrast to primates, tuned neurons are randomly interspersed in all rodents studied so far[11] (but see Ringach et al.[12]; Figure 1A). Since this "salt and pepper" organization is considered the most likely ancestral

state,[5,13–15] a fundamental transformation of V1 circuitry leading to the emergence of functional cortical columns must have marked the course of brain evolution in the primate lineage. Assuming a fixed minimal size of functional cortical columns, the total area of the cortex and the size of V1 are predicted to be critical variables in this transformation: below a certain V1 size, the reduced visual field coverage might outweigh the potential benefit of a columnar organization, thus favoring the salt and pepper organization.[14,16] But could cortical orientation columns perhaps be miniaturized? Recently, clusters of orientation-selective neurons were described in mouse V1, which might represent micro-scale precursors of full-fledge orientation columns.[12,15] We therefore asked whether V1 of the smallest living primate, the mouse lemur (Figures 1B and 1C), contains primate-type functional orientation columns and whether they may be miniaturized in such a small brain.

RESULTS

Mouse Lemur Visual Cortex Anatomy

We first determined the location and boundaries of the mouse lemur visual cortex. We performed cytochrome oxidase (CO) labeling on cortical flat mounts of three brains. We found that V1 is clearly delineated by a zone containing regularly spaced patterns of darker-stained CO patches, also known as CO blobs (Figures 1D and 1E). The patches were, on average, 269 μm (SD = 78.7 μm; n = 2 animals; 31 patches) wide and spaced by 485 μm (SD = 70.5 μm). This is similar to histological results in other primates,[5,20] yet it is markedly different from the homogeneous CO labeling found in rodents with equally sized or larger brains such as the agouti[21] or the gray squirrel.[22] In addition, we labeled coronal brain sections with antibodies against the vesicular glutamate transporter 2 (VGlut2) and the muscarinic receptor 2 (M2, Figure 1F). VGlut2 staining reveals the boundaries of V1 by dense labeling of the zone of thalamic afferents into the cortical layer IV[23] (L4). Similar to the CO staining, the supra-granular layers contained regularly spaced patches of VGlut2, confirming previous reports,[23] as well as overlapping M2 labeling (white arrows in Figure 1F). Taken together, our characterization of the mouse lemur V1 confirmed that it contains key anatomical hallmarks of primate V1 organization.

Orientation Preference Maps in the Mouse Lemur

Next, we asked whether V1 also contains functional orientation maps similar to the ones found in larger primates.[24,25] Initial electrode recordings by Cooper and colleagues[26] have already revealed a retinotopic organization of mouse lemur V1. We performed intrinsic signal imaging through a chronic cranial window positioned over V1 (Figure 1G; STAR Methods). Visual stimuli consisting of moving gratings oriented in eight different directions were presented to lightly anesthetized mouse lemurs on a computer screen. Intrinsic optical signals were quantified by comparing a baseline period with signals evoked during stimulus presentation. The subtraction of orthogonal directions revealed patterned responses of different intensities (Figures 2A and S2A). Angle maps of orientation preference demonstrate orientation domains arranged in a circular fashion, like a pinwheel, around center singularities.[27] The maps were stable across days of repeated imaging (Figures 2A, S1B, and S1C).

Next, we analyzed the spatial arrangement of the orientation domains. The spacing between fields responding to the same orientation, termed column spacing (Λ)[4,13] (Figure 2B), was, on average, 0.54 mm (mean; 95% confidence interval [CI]: [lower 0.5077, upper 0.6342]; n = 4 animals; Figure 2C). This is similar to the column spacing found in larger primate species such as the Galago[13] (mean 0.687 mm; CI: [0.5337, 0.7619]) and Macaque (two species: *Macaca mulatta* n = 7, *Macaca fuscata* n = 4; combined for analysis: mean 0.695 mm, CI: [0.5900, 0.7343]; Figure 2C), which is surprising considering the difference in brain and body size of up to two orders of magnitude.[29] These results indicate that orientation domain size only weakly scales with body or brain size in primates. This weak scaling also appears distinct from carnivore V1, for which substantial interspecies differences in column spacing Λ suggest a much stronger scaling with body and brain size (Figure S4). Our observations quantitatively exclude the possibility that the 50 μm iso-orientation clusters observed in mouse V1[12,15] represent allometrically scaled primate orientation domains. Primate V1 orientation domains appear only to weakly scale with body size and hence cannot be arbitrarily miniaturized.

Universal Pinwheel Arrangement across Primates

Even with an invariant column spacing, the typical size of individual orientation columns could be decreased in small brains by increasing the number of orientation pinwheels per hypercolumn area Λ^2, termed pinwheel density (ρ, average number of pinwheels per region of size Λ^2). It has been demonstrated previously that pinwheel density is predicted to be close to the mathematical constant π in models for the joint formation of the system of orientation domains and intracortical circuitry.[30] While this prediction has been confirmed across several mammalian species,[13,14,28] it remained unknown whether it applied to primate V1 in general. We thus examined the spatial organization of orientation domains and pinwheels in the mouse lemur and compared it to other primates and to mathematical models predicting a universal invariant pinwheel density. Are orientation domains and pinwheels arranged distinctly in mouse lemur visual cortex, or do they adhere to general design principles that universally apply to larger primates? To answer this question, we first calculated pinwheel density. Pinwheel density (r) was found to be indistinguishable between mouse lemur (mean 3.156; CI: [2.850, 3.376]) and other species including the galago (mean 3.332; CI: [2.698, 3.760]), a larger strepsirhine.[31] We also measured the pinwheel density in macaques (both species combined, mean 3.2447, CI: [2.850, 3.672]), which are simiiform primates. We found that in all these primate species spanning over two orders of magnitude in body size, the mean pinwheel density appeared invariant and matched the mathematical constant π (Figure 2D), the value predicted by models of large-scale circuit self-organization.[30,31] This analysis thus further corroborated that both V1 orientation domains and pinwheels cannot be arbitrarily miniaturized across primates.

To critically test the apparent universality of pinwheel arrangement across primates, we quantified further features of the arrangement of pinwheels across V1. We assessed their relative positioning within orientation hypercolumns by nearest neighbor distance distributions (same, opposite or independent of topological charge) for the mouse lemur and compared them to those of the macaque and the predictions of the universal design model[13] (Figure 2E). This analysis revealed that the means of the distributions were similar

(mouse lemur mean values: d = 0.357, CI: [0.343, 0.371]; macaque d = 0.349, predicted d = 0.359; mouse lemur $d^{+/+}$ = 0.518, CI: [0.502, 0.535]; macaque $d^{+/+}$ = 0.511, predicted $d^{+/+}$ = 0.525; mouse lemur $d^{+/-}$ = 0.389, CI: [0.372, 0.408], macaque $d^{+/-}$ = 0.396, predicted $d^{+/-}$ = 0.396). We also calculated pinwheel count fluctuations in subregions of V1 ranging from small regions up to subregions of 20 Λ^2 area (Figure 2E). Taken together, orientation maps in mouse lemur V1 were statistically indistinguishable from the macaque and closely adhered to universal design model predictions (Figure 2E).

Absence of Ocular Dominance Columns in Mouse Lemur

While the design of orientation domains and pinwheel arrangement in the mouse lemur was indistinguishable from other primates, including the macaque, their visual system might show qualitative differences in the integration of information from both eyes. Neurons driven by inputs from the left and right eye can be segregated in highly variable patterns[32] across primates, and in the macaque, such ocular dominance maps are arranged in alternating bands.[33] We therefore compared orientation-selective responses evoked by presenting visual gratings selectively to either the left or the right eye in the mouse lemur, but could not find any evidence for the occurrence of ocular dominance maps (n = 3 animals). Repeated observations across subsequent days yielded only weak and highly variable signals, probably due to random fluctuations (Figure S3). These observations expand the overall picture of a highly variable expression of ocular dominance across, but also within, some primate species[34] and might suggest a tendency to fuse left and right eye streams at the earliest cortical stage in the small mouse lemur brain. However, intrinsic signal imaging procedures may not be sufficiently sensitive to reveal ocular dominance maps. It may be needed to use more invasive methods, such as anatomical tract tracing or experiments involving monocular deprivations, to further probe this aspect of cortical architecture.

Mouse Lemur Visual Acuity

It has been hypothesized that the total number of processing modules such as pinwheels or orientation hypercolumns in V1 limits an animal's visual capabilities.[10,35] The small mouse lemur brain appears ideal to critically test this hypothesis. We thus estimated the visual acuity of the mouse lemur (Figure 3). We first quantified the optokinetic reflex (OKR) response. To evoke the OKR, horizontally moving vertical gratings of different spatial frequencies and contrasts were presented to the lightly anesthetized animal while tracking eye movements (Figure 3A; STAR Methods). The absolute contrast sensitivity was high, as expected for a nocturnal forager and hunter, and peaked at ~0.5 cpd (cycles per degree; Figure 3B). Since the optical performance under lightly anesthetized condition is not comparable to awake states, we also determined the visual acuity of mouse lemurs in a visual discrimination task (Figure 3C; STAR Methods; Video S1). We found that they could maximally resolve ~3 cpd at maximum contrast (Figure 3D, black line). The behavioral task measurements revealed slightly higher sensitivity compared to the OKR (Figures 3B and 3D, dotted line), yet probably still only represent the lower bound of the actual acuity. Taken together, these results suggest that the mouse lemur possesses a visual acuity similar to other arboreal, but diurnal, species such as tree shrews or gray squirrels (Figure 3D, adapted from da Silva Souza et al.[36]).

Large Relative V1 Size in the Mouse Lemur

We next assessed how the mouse lemur's visual acuity is related to V1 size (Figure 4). In a small primate brain, the large size of orientation domains (and estimated number of neurons per hypercolumn; Figure 4A) might limit the total number of pinwheels in V1 and hence directly affect the visual acuity. Srinivasan and colleagues[35] proposed that, across primate species, the total pinwheel number and visual acuity are proportional to each other (although not taking into account regional specializations such as the fovea). Given the mouse lemur's behavioral visual acuity of probably >3 cpd (Figure 3), their scaling relation predicts V1 to possess ~600 pinwheels per hemisphere. Fitting this number of pinwheels would require V1 to be exceptionally large in comparison to the rest of the cortex. Measuring the size of the mouse lemur V1 as identified by CO staining (Figures 1D and 1E), we found that it covers, on average, ~21% or ~48.9 mm^2 (±3.91; n = 6 [3 animals, both hemispheres]; Figure 4B) of the 227.6-mm^2 cortical surface per hemisphere (±22.11; n = 6), which is in line with previously published data.[29] Comparable measurements in macaques and humans showed that V1 covers only 10% or 3% of the cortex surface, respectively (Figure 4B, based on literature values[29,37]). This decrease of relative V1 size toward larger primates stands in stark contrast to rodent data where relative V1 size increases monotonically with neocortex size (Figure S4B). Calculating the number of pinwheels in the mouse lemur based on its V1 size, column spacing, and pinwheel density leads to an estimated number of ~550 pinwheels per hemisphere. This is close to the ~600 pinwheels predicted from visual acuity[35]. It also demonstrates that the mouse lemur V1 is not simply a scaled-down version of the macaque (Figure S4C). Instead, it covers a considerably larger fraction of the cortex compared to all other primates (Figure 4B) or equally sized rodents (Figure S4B) of similar visual acuity (Figure 3D).

DISCUSSION

In this work, we show that the mouse lemur brain contains robust orientation domains and pinwheels, despite possessing a brain size similar to that of rats. Although mouse lemur orientation domains are the smallest observed so far in any mammal, their weak scaling with body size suggests that primate orientation domains are nearly incompressible. Among primates, mouse lemurs exhibit one of the biggest V1-to-cortex ratios in line with the view that even the most basal primates are visual specialists. The finding that the different features of the orientation maps in the mouse lemur (which lack ocular dominance maps) are indistinguishable from other primates such as the macaque provides strong evidence for an invariant universal design of the orientation system across primates. This invariance contrasts with classical dimension reduction models,[38] which predict that the pinwheel densities would be substantially larger in the presence of strong ocular dominance[39,40] as well as with the highly variable layout and expression of ocular dominance columns across primates.[32]

A Lower Size Limit for Orientation Columns

What factors could set a lower size limit to orientation domains such that they cannot be scaled down with brain size arbitrarily? On the one hand, anatomical variables such as the typical range of dendrites and axons of cortical pyramidal cells or of connectivity with other

cell types might set a spatial scale for the formation of cooperative cell populations.[41] In this case, cell morphology may imply a limit size below which functional columns are not easily formed. Alternatively, computational models of V1 function indicate that local circuit operations are collective in nature and may thus require a minimum number of neurons for reliable function.[42–45] Intriguingly, estimating the number of neurons (based on the species-specific density; see STAR Methods) contained within an orientation hypercolumn (Λ^2 area[8,13]) across primate species converges on a near invariant count of about 8×10^4 (Figure 4A). Smaller primates are reported to have smaller neuron soma size[46] and higher neuronal density.[47,48] This relationship may account for the slightly smaller hypercolumn size observed in our data (Figure 2C). Interindividual variation in the size of orientation columns is under partial genetic control.[10] It is therefore conceivable that natural selection may have driven orientation columns in primates toward an optimized size. Future work should histologically confirm the actual number of neurons per hypercolumn, addressing how this number emerges and whether it satisfies a computational constraint imposed by information processing demands.

Unifying Accounts for V1 Architecture

Our results have multiple theoretical implications for V1 functional architecture, circuit organization, and its evolutionary emergence. First, our analysis revealed that the geometry of OPMs and pinwheel arrangements in the mouse lemur, the galago, and the macaque follow an extension of the “common design” framework.[13] It has been proposed that orientation columns and their universal organizing principles emerged independently in primates, their closest relatives, and in carnivores.[13] Notably, the common design framework is independent of the precise origins of orientation selectivity within cortical circuits, which are distinct in different lineages. A number of recent studies confirmed for various non-primates that orientation[49,50] and direction selectivity[51] emerge already in V1’s input layer IV and originate from the selective convergence of thalamic inputs. In primates, however, orientation selectivity is generated via an intracortical circuit, with input from orientation-unselective layer IV thalamo-recipient neurons.[52] Upper layer neurons then acquire orientation preference by selective convergence of inputs from layer IV.[53] Our finding of the weak scaling of orientation column size across primates and an apparently stronger scaling in carnivores further highlights that orientation columns in these two clades might be distinct structures that independently evolved to adhere to the same organizing principles. Second, a recent study proposed that the retino-cortical mapping ratio can separate species with OPMs from those without.[54] Given the mouse lemur V1 area (48 mm^2) measured in our study and the retinal area (130 mm^2) measured from flat mounts,[55] the hypothesis proposed by Jang et al. actually predicts the absence of OPMs in the mouse lemur, which is not supported by our data (Figure 2). Notably, the mouse lemur possesses a neocortex similar in size to the rat and a V1 size smaller than that of the squirrel and agouti (Figure S4A). These results suggest that additional factors apart from V1 size and retino-cortical mapping ratio govern the presence or absence of OMPs in the mammalian brain.

For instance, the functional implications of orientation columns versus salt and pepper have been frequently envisioned as a balance between minimizing wire length and maximizing

coverage.[7,8] It has been argued that the presence of orientation columns impairs the coverage of the visual field compared to salt and pepper. Orientation maps may represent an optimal solution in the case of large V1 in which columns and pinwheels are numerous and the cost of compromising feature coverage is low. Given a fixed minimal size of orientation columns, this impairment in general will be the more severe the smaller the V1 and is predicted to become prohibitive for very small areas[14,16,56] such as the 2-mm^2 V1 of the tenrec or the even smaller V1 of mesozoic stem eutherians.[14,57] Our finding that orientation columns and pinwheels cannot be scaled down arbitrarily strengthens this prediction. Future tests of the existence of a lower limit to the size of columnar visual cortices will need to focus on miniature mammalian brains outside the primate order.

Resolving the Evolutionary Origins of Primate Visual Cortex

The small size and basal phylogenetic position of mouse lemurs, and the many similarities of their biology, lifestyle, and habitat to the reconstructed euprimate ancestor, make them a promising model for studying V1 circuit evolution and the origins of primate vision in general.[3,58] Our observations increase the probability that the evolutionary emergence of primate-type V1 functional architecture occurred during a fundamental grade shift that overturned the euarchonta ancestral state in an all-or-nothing transition of becoming a visual specialist. If functional circuit structures intermediate in size between mouse iso-orientation clusters and primate-type orientation domains could be formed and maintained, the brain of the tiny mouse lemur would be a promising place to search for them. Instead, we found a full-fledged system of orientation domains and pinwheels practically indistinguishable from that of the macaque. Recently, Silcox and coworkers argued that the final steps in the evolution of stem primates must have consisted of a substantial encephalization burst that had no analog in rodents[59] and that was coupled to the frontal repositioning of the primate eye.[58] It would be parsimonious to assume that the primate-typical large and columnar V1 emerged during this vision-related encephalization burst. Given that pinwheels cannot be arbitrarily miniaturized and the close relation between pinwheel number and visual acuity, it is tempting to conjecture that selection for visual performance drove a massive size expansion of V1 near the origin of primates.

Mouse Lemurs as a Primate Model for Systems Neuroscience

As a primate model for systems neuroscience, the mouse lemur has many advantages, including that most experimental tools developed for mice are potentially transferable. Indeed, our results illustrate that optical methods, such as intrinsic signal imaging through chronic cranial windows can be easily adapted. This is a promising first step toward analyzing single-cell responses within primate cortical circuits using high-density electrophysiology or chronic two-photon calcium imaging.[60] Such experiments will potentially allow us to gain a better understanding of how V1 processing differs between rodents and primates at the single-cell level. Notably, mouse lemurs are so far the only primate species in which fitness proximal traits can be correlated with individual cognitive capabilities in the wild.[61] The ease of breeding in captivity,[62] as well as short gestation (2 months) and quick maturation (1 year[63]), allows studying mouse lemurs in controlled laboratory settings without compromising the wild population. Understanding the circuit basis of ecologically relevant mouse lemur behaviors may thus potentially reveal the

adaptive value of primate-specific neuronal information processing principles. For us to learn these lessons, it will however remain critical to protect the integrity of the threatened ecosystems that sustain them in the wild.[64]

STAR★METHODS

RESOURCE AVAILABILITY

Lead Contact—Further information and requests for resources and reagents should be directed to and will be fulfilled by the Lead Contact, Daniel Huber (daniel.huber@unige.ch)

Materials Availability—This study did not generate new unique reagents

Data and Code Availability—Datasets generated and codes used in this study are available in the research data repository of the University of Geneva: https://yareta.unige.ch/ https://doi.org/10.26037/yareta:n2u7jm3wf5he7p6xpecta4gktm

EXPERIMENTAL MODEL AND SUBJECT DETAILS

Adult mouse lemurs (8 males and 4 females) between the ages 1–2.5 years were used in this study. All experiments were carried out with individuals bred and raised in the “Mouse Lemur Platform” (authorization number E-91-114-1) of the “Museum National d’Histoire Naturelle” in Brunoy, France (UMR MECADEV CNRS/MNHN 7179,). Animals sacrificed for this study were specifically bred for biomedical research purposes and did not affect the overall breeding and conservation programs of the facility. Whenever possible, the animals were returned to the colony after the experiments. All experimental procedures were in accordance with European animal welfare regulations and were reviewed by the local ethics committee (“Comité d’ éthique en expérimentation animale No. 68”) in Brunoy, France, by the ethics committee of the University of Geneva, Switzerland and authorized by the French “Ministère de l’éducation nationale de l’enseignement supérieur et de la recherche.”

METHOD DETAILS

Behavioral contrast sensitivity—To behaviorally determine the contrast sensitivity of mouse lemurs, we trained two young adult males (see Table S1) in a left/right discrimination task. Stimuli consisted of stationary vertical gratings of various contrasts (1 to 0.01) presented in blocks of 40 trials and spanned half the screen (Dell P2414H, 1920×1080,60Hz), either on the right or left side in a pseudo-random order. The other half of the screen was set at a gray level with matched luminance. The correct choice would consist of entering the lick port on the side where the grating was presented. Each session consisted of blocks from one single spatial frequency (between 0.25 and 3 cycles per degree). Contrasts were converted into contrast sensitivity values via the equation: $1/((I_{max}-I_{min})/(I_{max}+I_{min}))$, where Imax and Imin are the maximum and minimum luminance of the stimuli as measured by a lux meter, which was fitted by a power function. One day before and during the days of the experiments, food availability was restricted to the rewards obtained during the session. Animals were allowed to perform until satiated or until they stopped engaging in the task. If their weight dropped below 60 gr, animals were

supplemented with additional food until they reached 60 gr. The standard liquid diet[69] was used as rewards and food supplements.

A custom made behavior box with three lick-ports (Sanworks) was used for the experiment. The animals viewed visual stimuli on a computer screen (Dell P2414H, 1920×1080, 60Hz, set at 50% brightness, distance 30 cm) through a transparent Plexiglas window on which the three lick-ports were mounted. There was no additional light provided. The animals were trained to initiate visual stimulus presentation by a nose poke at the center port for 300 ms. They were rewarded with liquid food by poking into the left or right lick-port according to the stimulus presented.

Optokinetic reflex—To assess the optokinetic reflex response we used the visual rotations of a virtual drum. The visual stimulus consisted of vertical black and white stripes of different spatial frequencies and contrasts. The stimulus was generated using the PsychoPy python library on the 27 inch monitor (ASUS PG278QR, 165 Hz refresh rate, 2560 by 1440 pixel, 1 ms response time) placed at a 45 cm viewing distance. Before transmission to the display, each frame was virtually projected to a cylindrical surface giving the impression of a rotating drum centered on the animal's viewpoint. For each tested pair of spatial frequency and contrast values, the velocity profile of the drum motion consisted of two sinusoidal cycles at 0.05 Hz and always covered the same angular amplitude. Animals (n = 3) were administered with buprenorphine (0.3ug/g) and briefly anaesthetised with isoflurane. They were subsequently positioned in a body harness in front of the screen and allowed to wake up from isoflurane anesthesia. Buprenorphine sufficiently sedated the animals to gain stable recordings. The eyes were recorded with a 1/3" CMOS camera (Firefly MV FMVU-03MTM, Point Grey Research). Custom video acquisition software programmed in MATLAB (Mathworks) saved 8-bit greyscale images (376 × 240 pixels) to disk at a variable rate with mean » 60 frames/s. The time stamps relative to trial onset of each frame were saved in the image headers. We used the DeepLabCut toolbox[66] to track the position of the upper and lower extremities of the lemur's left eye pupil and took their average as an estimate of eye position in video frame coordinates (i.e., pixel units). The eye position trace was up-sampled for analysis to a fixed 100 Hz sampling rate using linear interpolation. We identified the quick phases of ocular nystagmus (or spontaneous saccades) based on an eye acceleration threshold (1000 pixels/s2). The start and end of each quick phase was subsequently identified using a velocity threshold (10 pixels/s). The quick phase (and saccade) periods were removed from the eye position trace and the remaining slow phases low-pass filtered with a Savitzky-Golay filter (degree = 1, window = 10 samples). To estimate the size of the evoked optokinetic reflex, we fitted the slow phase velocity trace with a sinusoidal function with the frequency parameter fixed at 0.05 Hz (i.e., the stimulus frequency) and amplitude and phase as the free parameters using the method of non-linear least-squares. The fitted amplitude parameter was taken as a measure of the optokinetic reflex size.

Histology—Anesthesia was induced with 5% isoflurane in oxygen, followed by an intraperitoneal (IP) injection of pentobarbital (150mg/kg). The animals were transcardially perfused with approximately 60ml 1X Phosphate Buffer Saline (PBS) followed by 60ml

of paraformaldehyde (PFA, 1% for flatmounts, 4% for coronal sections) in 1X PBS. For flatmounted sections, the cortex was isolated and flattened based on a modified protocol originally for the macaque brain[70] immediately after perfusion. To isolate the cortex, the brain was first partitioned into its two hemispheres by cutting along the midline with a scalpel. The brainstem and cerebellum were removed by carefully inserting a rounded spatula between the cortex and the cerebellum. The midbrain structures are pried apart and peeled away from the cortex at the level of the corpus callosum. White matter tracts holding the posterior pole in shape are removed to allow unfolding of the occipital lobe. Next the temporal lobe was unfolded while removing the white matter tracts beneath. White matter surrounding the sylvian sulcus was removed as much as possible and a cut was made along the sulcus and the whole cortex was unfolded. The unfolded cortex was then transferred and sandwiched between two glass slides and covered with 4% PFA. A steady pressure was applied on the top glass slide for approximately 20 s. All specimens were post-fixed in 4% PFA overnight at 4°C and cryo-protected by sinking in 20% sucrose in 0.1M phosphate buffer (PB) or 1X PBS prior to sectioning. Coronal sections were cut at 50μm. Flat-mounted sections were embedded in OCT compound (Cell Path; KMA-0100–00A) and cut at 80–100μm with a freezing sliding microtome (Microm, HM430). Coronal sections were collected into 10 separate series spanning the whole brain at 500μm intervals between sections within a series.

Immunofluorescence: After initial rounds of 3 × 10 min washes in a base buffer containing 0.3% Triton X-100 in 0.1M PB, specimen slices were first treated with 3% bovine serum albumin (Sigma A3059) in base buffer for 1 h at room temperature. After blocking, they were incubated in with the primary antibody at 4°C. For muscarinic receptor 2, monoclonal IgG2a rat α-m2 AchR (1:500; Millipore MA367 1mg/mL) antibodies was used for overnight incubation. Following rinsing for 3 rounds of 10 min in base buffer, the slices were incubated with goat α-rat linked with Alexa Fluor 594 (1:250; Invitrogen A11007) and 1.5% BSA in base buffer for 2.5 h at room temperature in the dark. For vesicular glutamate receptor 2 (VGlut2), incubation with the primary antibody polyclonal guinea pig α-VGlut2 (1:2000; Millipore AB2251 1mg/mL) or polyclonal rabbit α-VGlut2 (1:1000; Synaptics System, SySy135403 1mg/mL) with 1.5% BSA in base buffer took 24 h at 4°C. Subsequent to 3 rounds of 10 min rinsing, the slices were incubated with goat α-guinea pig Alexa Fluor 594 (1:200; Invitrogen A11076) or goat α-rabbit Alexa Fluor 488 (1:200; Invitrogen A11034) in base buffer for 2 h at room temperature in the dark. Slices were then washed in base buffer for 3 times 10 min each before subsequently counter-stained with DAPI (Thermo Fisher D1306) in the dark and mounted on glass slides with fluoromount (Sigma Aldrich F4650). Sequential brain slices were taken for VGlut2 and M2 immunofluorescence.

Double immunofluorescence against VGlut2 and M2 were carried out using a primary antibody mix of rabbit α-VGlut2 (1:1000; Synaptics System, SySy135403 1mg/mL) and α-m2 AchR (1:500; Millipore MA367 1mg/mL) in 1.5% BSA in base buffer at 4°C for 24 h. For the secondary antibody incubation, slices were incubated in a mixture of goat α-rat Alexa Fluor 594 and goat α-rabbit Alexa Fluor 488 (both 1:250) and 1.5% BSA in base buffer at 4°C for 12 h in the dark.

Cytochrome oxidase histochemistry: Cytochrome oxidase (CO) histochemistry was carried out based on a standard protocol.[71] After three rounds of washing in 0.1M PB for 5 min, slices were bathed in a cocktail of cytochrome *c* (0.4mg/mL; Sigma-Aldrich C2506), sucrose (0.1g/mL), diaminobenzidine (0.7mg/mL; SigmaFast D4293) dissolved in 0.1M PB solution, for around 12 to 18 h at 4°C or until the desired staining intensity was reached. The slices were allowed to dry on glass slides covered by a Petri dish overnight for dry mounting. All widefield and fluorescence imaging were carried out on a Zeiss Axioscan.Z1 slide scanner. Image processing was first performed in ImageJ before determining regions or points of interest. Data was subsequently imported to MATLAB 2018a for quantitative analysis.

Intrinsic signal imaging (ISI)—For the mouse lemur, four adults (three males and one female) between 1.5–2.5 years old, underwent surgical procedures to implant a cranial window. All surgical procedures were performed under strict sterile conditions and according to European and Swiss animal welfare regulations. Anesthesia was induced by subcutaneous Buprenorphine injection and followed by ~5% Isoflurane (in oxygen). Dexamethasone, Carprofen and Ceftriaxone were administered intramuscularly prior to the surgery. Animal was placed in a custom made stereotaxic frame. The eyes were protected with Lacryvisc and the tongue was covered with a thin layer of Vaseline. The area for the surgical procedure was shaved and was subsequently disinfected with 70% Ethanol, Betadine and Chlorhexidine 1%. Lidocaine was administered subcutaneously. During the surgery breathing rate and reflexes were continuously monitored and the anesthesia levels were adjusted accordingly. The skull was exposed and a titanium bar was attached to the dried bone with cyanoacrylate glue (ERGO 5011). ECoG electrodes were implanted over frontal and visual cortex contralateral to the craniotomy (to determine anesthesia levels during the experiments). A craniotomy of 6mm diameter was performed over the visual cortex and a double layered glass window was inserted to replace the bone.[72] Finally, the window and titanium frame were sealed with transparent dental acrylic (Lang Dental). The animal was administered analgesic treatment (Buprenorphine, 0.1mg/kg) for the following week and antibiotics (Ceftriaxone, 20ul of 1g in 5ml Lidocaine) for 9 days. For the *Macaca fuscata*, the method for performing ISI has been described in detail in a previous publication.[73]

ISI experimental setup—To perform intrinsic signal imaging the animals were lightly anaesthetized. Anesthesia was induced by subcutaneous buprenorphine injection and followed by ~5% isoflurane. The animal was positioned 20–25 cm from the LCD screen (Dell P2414H, 1920×1080, 60Hz) where full-screen gratings were shown. The head was stabilized by tightly clamping the titanium bar on both sides. The body temperature was controlled using a homeothermic blanket system (Harvard Apparatus). The cranial window was illuminated initially by green 515 nm LED in order to acquire the blood vessel map and followed by 620 nm red LED illumination for the rest of the experiment. Light anesthesia was kept at 0.2%–1.5% isoflurane (in oxygen) based on ECoG signal which was monitored during the entire experiment. Buprenorphine induction at the start of the experiment allowed isoflurane anesthesia to be more stable and at lighter levels. Spontaneous blinking and sporadic eye closures were sufficient to keep the eyes moist. Pre-amplified ECoG was

further amplified by Cornerstone Dagan EX4–400 (differential, 500x, 0.3 highpass and 300Hz lowpass filtered). Online ECoG was monitored with a Rigol DS1074 oscilloscope. LED's were powered by a stabilized PeakTech laboratory power supply (6080) at 3.6V at 0.2–0.6mA. The animal and stimulation settings were continuously monitored using three infrared video cameras (Firefly MV FMVU-03MTM, Point Grey Research). Luminosity of the visual stimulus screen was continuously measured with a photodiode (ThorLabs PDA 100A-EC). A National Instruments NI USB-6341 data acquisition board was used to generate pulses in order to synchronously trigger all cameras and data acquisition.

Visual stimuli consisted of black and white bars of 0.16 cycles per visual degree. Drifting bars in eight different directions were presented in a pseudo-random order (four orientations, each in two directions at 4 cycles per second). Each trial was composed of a 2 s pre-stimulus period, a 4 s stimulus and a 4 s post-stimulus period. During pre- and post-stimulus period animal were exposed to a gray screen which was adjusted in brightness to match the brightness of the stimulus. One experimental session contained up to 10 blocks of 40 trials. After the experiment the animal was handled until it fully recovered from anesthesia and it was returned to the home cage. The repeated chronic imaging allowed us not only to gain more accurate data, but also reduce the total number of animals used (see Table S1).

ISI data was acquired using a Retiga Ex monochrome 12-bit camera (QImaging). Data output in the form of RAW frames was acquired at 10Hz, 800×600 pixels resolution and spatial binning factor of 2 using EPHUS software. In order to achieve optimal focus and zoom on the cranial window, the camera is equipped with a double lens system (f = 105mm, f 2.5 and f = 55mm, f 3.5, both Nikon.[74]

Data Inclusion and Exclusion—All experimental animals were included in the analysis. Intrinsic imaging sessions with high movement artifacts or low signal-to-noise were excluded from analysis. Stimulus conditions in the behavioral task with less than 35 trials pooled across all sessions were excluded from analysis due to low number of repeats. One CO-stained flatmount was excluded from calculation of CO blob nearest neighbor distances due to lower quality of the tissue, containing numerous micro-fractures, which prevented precise localization of the centers of CO blobs.

QUANTIFICATION AND STATISTICAL ANALYSIS

Determining visual acuity from behavior contrast sensitivity—Data for each animal were pooled across sessions. The criterion performance was calculated based on a binomial distribution (p(success) = 0.5, one tailed) to determine threshold contrasts for each spatial frequency. Threshold contrasts across spatial frequencies were averaged across the two animals tested and a Gaussian fit to the log(contrast sensitivity) against spatial frequency was made to obtain an averaged contrast sensitivity curve (Figure 1).

Determining visual acuity from optokinetic reflex—Statistical significance was assessed using a bootstrapping method, as follows. For each trial, 1999 datasets each comprising a random sample of half of the eye velocity data points were used for fitting and the sets comprising the other half for cross-validation. The fraction of the 1999 estimates of explained variance with cross-validation sets that were more extreme than zero was

defined as the p value. An optokinetic reflex response was deemed to be significant at the $p < 0.01$ level. For each spatial frequency, the size of the optokinetic reflex (i.e., the fitted amplitude parameter) was plotted as a function of the logarithm of contrast and fitted with an exponential function. At a given spatial frequency, the contrast value at which the exponential fit exceeded the average of the non-significant sizes by a factor of two was defined as the contrast threshold. Contrast values were converted to contrast sensitivity in the same manner as the behavioral contrast sensitivity, a power function was applied to convert contrast to contrast sensitivity. Visual acuity was defined as the contrast sensitivity at the contrast threshold.

VGluT2 and M2 overlay—Consecutive sections were aligned by rigid transformation using patterns of blood vessels identified in both sections and the resulting alignment was verified by eye. To assess patch colocalization between VGlut2 and M2, rectangular regions of interest of fixed size were drawn over VGlut2 patches tangent to L4. Pixel intensities were first normalized via dividing by the mean intensity across the region of interest. An intensity profile was obtained by averaging across normalized pixel intensities in a line perpendicular to the tangent. The corresponding intensity profile for the same region of interest in the M2 channel or for the consecutively aligned M2 stained slices was similarly obtained. A mean intensity profile was calculated by averaging over all regions of interest for each staining. These mean profile plots were subsequently compared.

CO patch nearest neighbor distances—For the CO histochemistry preparation, the patches and their centers were identified by eye after adjusting contrast. The nearest neighbor distances were calculated for the visually identified centers. Kruskal-Wallis analysis of variance for non-parametric data was performed to compare nearest neighbor distances across animals. No significant differences were found between animals, hence the data were pooled across animals and the mean and standard deviation computed.

ISI raw data pre-processing

Data extraction: For each experiment session around 60 normalized response images to each stimulus condition were extracted together with 60 blank response images. The images were obtained as follows:

B - response to blank stimulus: Blank response images were extracted by averaging 10 frames (1 s) before stimulus onset for each presentation.

So - baseline signal: The blank response images corresponding to each full set of stimuli (e.g., 8 drift directions) were averaged to calculate the baseline So. This baseline was calculated separately for each new full set of stimuli presentations.

S - response signal: For each stimulus presentation 4 response images were obtained by averaging 10 frames (1 s) each starting two seconds after stimulus onset and continuing until 2 s after stimulus conclusion.

D - normalized response signal: The extracted data was calculated using $D = - (S - So)/So$. The minus sign came because in intrinsic signal imaging an increase in neural

activity results in a decrease in signal, measured as an increase in blood oxygenation (following a short initial decrease in oxygenation) which absorbs more light.

Image registration across sessions

Manual alignment: The initial alignment was obtained by manually selecting matching reference points between the sessions from the image of the blood vessels. With the points an affine transform matrix was calculated which was constrained to scaling, rotation and translation. The blood vessels image was obtained performing a PCA of the blank responses and selecting the component where the vessels are more visible.

Automated refinement.: To refine the manual alignment the next steps were based on the structure of the orientation map itself. The procedure to calculate the orientation map from the data of the session is detailed further below:

The first automated method calculated the affine transform that minimizes the distance between corresponding pinwheels in a pair of sessions, again only allowing global translation, rotation and scaling. Pinwheels were marked at the intersection of the zero contours of the real and imaginary components of the complex valued orientation map (see below). Matching pinwheels between the sessions were calculated based on their distance and sign (clockwise or anti-clockwise increase of orientation preference around the center, i.e., topological charge). To increase the possible displacement radius of the pinwheels, the initial and final maps were linearly interpolated and the pinwheels matched iteratively.

The second automated method calculated the affine transform that minimized the dissimilarity of the spatial structure of the orientation maps. The cost function to minimize was the average of the absolute orientation difference between the pixels of the sessions.

Region of interest (ROI) definition: The ROI was manually defined based on the following reference images:

1. A high-pass filtered orientation map, indicating visually responsive areas.
2. The sum of the normalized cardinal and oblique responses (real and imaginary part of the complex valued orientation map). This image clearly displayed response modularity and helped to determine activity boundaries.
3. The image of the vasculature, as obtained in the alignment procedure. This was used to avoid areas that could potentially suffer from blood vessel artifacts.
4. The pixel-wise coefficient of variation (CV) of the orientation map, which helps to identify areas with low signal to noise ratio. The variance of the orientation map for the CV was calculated from the difference of the measured map and 100 bootstrap samples of the data (see below).

Band-pass filter cutoff settings

Manual definition: To define the high-pass cutoff and an initial low-pass cutoff frequencies the radial profile of the 2D power spectrum of the orientation map was calculated, where the x axis was inverted to show the scale in millimeter instead of the wavenumber k. When

the map was of good quality, the power was low for small scales, rapidly increased around 0.4–0.8 mm to a few large peaks corresponding to the typical scale of the map, decreased afterward and started fluctuating depending on the larger structures of the layout. The initial low-pass cutoff was set where the first peak starts raising. The high-pass cutoff was set where the first peaks had dropped and before the power rises again. Both settings were selected using the information of all sessions and are unique to each animal.

Automated refinement: To further refine the low-pass cutoff, the setting was selected for which the number of pinwheels and their location was minimally changing when its value was perturbed. To get this value for each pixel a curve is measured of how the local pinwheel density (pinwheel count inside the local hypercolumn size) decreased as the low-pass cutoff was increased. For most pixels this decrease was linear except at a constant plateau in a given cutoff range, representing the settings where locally the map was minimally changing. First the plateau range was extracted for each pixel by piecewise fitting. Then the low-pass cutoff that was included in the majority of the pixel's plateaus was selected. As with the manual definition, the refined low-pass used the information of all sessions combined and is unique to each animal.

Orientation map calculation: The orientation maps from the normalized response data D (see data extraction) were calculated by first averaging the images of the responses across stimulus repetitions such that a single image for each condition was obtained. The images were then combined in a circular average, where each image was multiplied by a complex number exp(i*theta), with theta twice the orientation of the corresponding drifting grating. The obtained map was normalized by subtracting the mean and dividing by the standard deviation of the pixels inside the defined region of interest. The resulting orientation map was complex valued, where the phase defines twice the preferred orientation and the magnitude of the orientation selectivity.

Filtering: The resulting orientation map was band-pass filtered in Fourier space. The 2D Fourier transform of the complex orientation map was multiplied by a combination of logistic functions that switch radially at the defined frequency cutoffs between 0 and 1. The steepness parameter of the functions was set to 5% of the respective cutoff frequencies. To account for potential boundary effects, the filtered map was normalized by the result of applying the same filter to the region of interest.

Bootstrap samples: For each bootstrap sample the normalized response images D were re-sampled with replacement for each stimulus condition independently until the same number of images as the original data were gathered. The resampled data was combined to generate a bootstrap sample of the orientation map and is processed as described above.

Denoising: To increase the signal to noise ratio of the orientation maps, an implementation of the 'Generalized Indicator Functions' method was used.[75] The method gets as input the normalized response, data D and returns a family of images that simultaneously maximized variations between stimulus conditions and minimized variations inside each stimulus condition. Projections of the data to this family of images with signal to noise ratio above a given threshold were returned and further used to generate orientation maps

as described above. This procedure was not used when variations between the bootstrap samples of the data are calculated, since resampling leads to repetitions of the same images in the input data and therefore virtually the same output. In those cases an implementation of the 'Local Similarity Minimization' method was used.[76] The method uses a set of images representing potential artifacts as templates and minimizes the neighborhood similarity from the normalized response data D. The templates are obtained from a PCA of the blank response images.

Ocular dominance calculation: To extract potential ocular dominance maps, recordings to ipsilateral and contralateral monocular stimulations were combined. First each recording was processed separately as described above, obtaining two sets of normalized response data D_ipsi and D_contra (see data extraction). For each set the response to the different stimulus conditions in each trial were averaged, obtaining a single cocktail blank image per trial. The set of cocktail blanks for ipsi and contralateral stimulation were passed through the 'Generalized Indicator Functions' algorithm,[75] see Denoising above), maximizing the separation of the monocular response signals. The ocular dominance response was then obtained by averaging the resulting projection for each condition and then subtracting each other.

This procedure was tested successfully in intrinsic signal imaging datasets of cats, ferrets and macaques coming from different imaging experiments. In those datasets this approach showed to be more reliable and obtain better results than subtracting the orientation selectivities of the ipsilateral and contralateral stimulated orientation maps or variations thereof.

Orientation map design statistics

Column spacing estimation: To calculate a 2D map of the local column spacing the wavelet method introduced previously was used.[68] Morlet wavelets with 16 orientations and varying spatial sizes were generated and convolved with the real and imaginary part of the complex orientation map separately. These correspond to maps obtained from the subtraction of single response patterns, i.e., (horizontal: 0deg - 90deg) and (oblique: 45deg - 135deg). The so called difference maps have no pinwheels, but show the periodicity measured in orientation maps. For each wavelet size, which varied between 0.3 mm to 1.1 mm in steps of 0.05 mm, the magnitude of the resulting convolution was averaged over the wavelet orientations. With this information, for each pixel a curve of wavelet size versus averaged convolution magnitude was obtained. This curve was interpolated to increase its resolution. The pixel's column spacing was determined by finding the value where the curve is at its maximum. The results of using the real and the imaginary part of the orientation map were averaged to get the final local column spacing and the average spacing was obtained by averaging the values inside the region of interest.

Pinwheel statistics calculation—To estimate the pinwheel density and other pinwheel layout parameters a fully automated procedure proposed in a study by Kaschube and colleagues[13] was used. We refer to the Supplemental Material of that paper for further

details. MATLAB code to run this analysis is published in the Supplemental Material of Schottdorf's study.[28]

Confidence intervals for the column spacing and pinwheel density were calculated via bootstrapping as parametric tests were inappropriate since normality of the distribution and similarity of the variances cannot be assumed (due to the low number of animals and cross species comparison). As such, for each animal, a vector of column spacing for each pixel was created, which was bootstrapped 100 times, and the mean calculated. The sampled mean for all animals in a species were combined with the 95% confidence interval obtained from the resulting distribution. For the macaques, the two species *Macaca mulatta* and *Macaca fuscata*, were combined in order to sample from a larger number of animals.

Calculation of the V1/Neocortex ratio and volumes—The V1:Neocortex ratio was calculated based on area estimates from VGluT2 labeled coronal sections taken throughout the brain of 3 animals.for both hemispheres. In two animals, the interslice distance was 250μm while in the third one the interslice distance was 500μm. The length of cortical L4 was measured for each slice and the area of was interpolated between adjacent slides using the trapezium method. Cortical L4 was chosen as V1 could be delineated with ease due to the VGluT2 labeling described above. The area of V1 was divided by the area of the cortex to derive the ratio. The area V1/Neocortex ratio from the mouse lemur from the current study corresponded well with the volume ratio in Stephan et al.[29] For better comparison, the V1/Neocortex ratio of primates in Figure 3C were calculated from volume measures from Stephan et al. which were given for the whole brain (ie. both hemispheres).[29] For rodents, the values were less readily available from the literature. The mouse neocortex volume, V1 volume and ratio data were taken from a study from Herculano-Houzel et al.[77] Note that these volume values are for one hemisphere. From literature the values for the rat neocortex volume[78] and the ratio[79] were obtained. Similarly, the squirrel neocortex volume[80] and the ratio[79] sourced from previous literature. Neocortex volume of the agouti was calculated by multiplying the cortical flat-mount area[81] with cortical thickness.[21] The agouti V1/Neocortex ratio was measured from a published cortical flat-mount.[81] The capybara neocortex volume was taken from a study by Campos and Welker[82] and the ratio was measured from a schematic diagram found in the same study. Note that the diagram was not of a flat-mount, but more akin to the dorsal view and does not take into account the gyrification found in the capybara cortex. In addition, extrastriate areas were likely to be included in the visual area of the capybara, since visual cortex was determined by electrophysiological response to brief light flashes. Hence the ratio is likely an overestimate and less reliable compared to the values of better studied species. It was nonetheless included for comparison as the capybara is the largest rodent in the world.

Number of neurons per hypercolumn: The number of neurons per hypercolumn calculated by: number of neurons = (surface neuronal density) x (column spacing).[2] Surface neuronal density: Mouse lemur calculated by multiplying neuronal density (neurons per mm^3)[83] by V1 volume[29] and dividing by V1 area (this study: 48.9mm^3). All others from.[84] Note the surface density for the binocular region of the treeshrew was used for calculation. Column spacing: human,[37] marmoset,[85] galago,[13] tree shrew.[13]

Number of pinwheels and hypercolumns in V1: The number of pinwheels in V1 was estimated by: number of pinwheels = V1 area x pinwheel density / column spacing 2.

The number of hypercolumns in V1 was related to number of pinwheels by: number of hypercolumns = number of pinwheels / pinwheel density

Supplementary Material

Refer to Web version on PubMed Central for supplementary material.

ACKNOWLEDGMENTS

We would like to thank Siegrid Löwel and Matthias Kaschube for their advice and guidance on V1 intrinsic signal imaging, and Leonard White, Kevan Martin, and Mary Silcox for their comments on the manuscript. We would like to express our gratitude to Martine Perret and the animal caretakers at the Brunoy facility for their help with mouse lemur handling and breeding, and the members of the Huber lab for their support and discussions.

This work was supported by the Human Frontiers Science Program (D.H. and F.P., RGP0024/2016), the New York Stem Cell Foundation (D.H.), the German Research Foundation (F.W., CRC 889; F.W. and D.H., PP2205), the Volkswagen Foundation (F.W., ZN2632), the Ministry for Science and Culture of Lower Saxony, and Max Planck Society (F.W.). D.H. is a New York Stem Cell Foundation-Robertson Investigator.

REFERENCES

1. Churakov G, Sadasivuni MK, Rosenbloom KR, Huchon D, Brosius J, and Schmitz J (2010). Rodent evolution: back to the root. Mol. Biol. Evol 27, 1315–1326. [PubMed: 20100942]
2. O'Leary MA, Bloch JI, Flynn JJ, Gaudin TJ, Giallombardo A, Giannini NP, Goldberg SL, Kraatz BP, Luo ZX, Meng J, et al. (2013). The placental mammal ancestor and the post-K-Pg radiation of placentals. Science 339, 662–667. [PubMed: 23393258]
3. Kaas JH (2013). The evolution of the visual system in primates. In The New Visual Neurosciences, Werner ALCJ, ed. (MIT Press), pp. 1233–1246.
4. Hubel DH, and Wiesel TN (1974). Sequence regularity and geometry of orientation columns in the monkey striate cortex. J. Comp. Neurol 158, 267–293. [PubMed: 4436456]
5. Kaas JH (2012). Evolution of columns, modules, and domains in the neocortex of primates. Proc. Natl. Acad. Sci. USA 109 (Suppl 1), 10655–10660. [PubMed: 22723351]
6. Ohki K, Chung S, Ch'ng YH, Kara P, and Reid RC (2005). Functional imaging with cellular resolution reveals precise micro-architecture in visual cortex. Nature 433, 597–603. [PubMed: 15660108]
7. Koulakov AA, and Chklovskii DB (2001). Orientation preference patterns in mammalian visual cortex: a wire length minimization approach. Neuron 29, 519–527. [PubMed: 11239440]
8. Hubel DH, and Wiesel TN (1977). Ferrier lecture. Functional architecture of macaque monkey visual cortex. Proc. R. Soc. Lond. B Biol. Sci 198, 1–59. [PubMed: 20635]
9. Hubel DH, and Wiesel TN (1974). Uniformity of monkey striate cortex: a parallel relationship between field size, scatter, and magnification factor. J. Comp. Neurol 158, 295–305. [PubMed: 4436457]
10. Kaschube M, Wolf F, Geisel T, and Löwel S (2002). Genetic influence on quantitative features of neocortical architecture. J. Neurosci 22, 7206–7217. [PubMed: 12177215]
11. Ohki K, and Reid RC (2007). Specificity and randomness in the visual cortex. Curr. Opin. Neurobiol 17, 401–407. [PubMed: 17720489]
12. Ringach DL, Mineault PJ, Tring E, Olivas ND, Garcia-Junco-Clemente P, and Trachtenberg JT (2016). Spatial clustering of tuning in mouse primary visual cortex. Nat. Commun 7, 12270. [PubMed: 27481398]

13. Kaschube M, Schnabel M, Löwel S, Coppola DM, White LE, and Wolf F (2010). Universality in the evolution of orientation columns in the visual cortex. Science 330, 1113–1116. [PubMed: 21051599]
14. Keil W, Kaschube M, Schnabel M, Kisvarday ZF, Löwel S, Coppola DM, White LE, and Wolf F (2012). Response to Comment on "Universality in the Evolution of Orientation Columns in the Visual Cortex". Science 336, 413–413.
15. Kondo S, Yoshida T, and Ohki K (2016). Mixed functional microarchitectures for orientation selectivity in the mouse primary visual cortex. Nat. Commun 7, 13210. [PubMed: 27767032]
16. Kaschube M (2014). Neural maps versus salt-and-pepper organization in visual cortex. Curr. Opin. Neurobiol 24, 95–102. [PubMed: 24492085]
17. Seiffert ER, Tejedor MF, Fleagle JG, Novo NM, Cornejo FM, Bond M, de Vries D, and Campbell KE Jr. (2020). A parapithecid stem anthropoid of African origin in the Paleogene of South America. Science 368, 194–197. [PubMed: 32273470]
18. Zhang M-L, Li M-L, Ayoola AO, Murphy RW, Wu D-D, and Shao Y (2019). Conserved sequences identify the closest living relatives of primates. Zool. Res 40, 532–540. [PubMed: 31393097]
19. Huchon D, Chevret P, Jordan U, Kilpatrick CW, Ranwez V, Jenkins PD, Brosius J, and Schmitz J (2007). Multiple molecular evidences for a living mammalian fossil. Proc. Natl. Acad. Sci. USA 104, 7495–7499. [PubMed: 17452635]
20. Preuss TM, Qi H, and Kaas JH (1999). Distinctive compartmental organization of human primary visual cortex. Proc. Natl. Acad. Sci. USA 96, 11601–11606. [PubMed: 10500223]
21. Dias IA, Bahia CP, Franca JG, Houzel JC, Lent R, Mayer AO, Santiago LF, Silveira LCL, Picanço-Diniz CW, and Pereira A (2014). Topography and architecture of visual and somatosensory areas of the agouti. J. Comp. Neurol 522, 2576–2593. [PubMed: 24477926]
22. Wong P, and Kaas JH (2008). Architectonic subdivisions of neocortex in the gray squirrel (Sciurus carolinensis). Anat. Rec. (Hoboken) 291, 1301–1333. [PubMed: 18780299]
23. Saraf MP, Balaram P, Pifferi F, Gămănuţ R, Kennedy H, and Kaas JH (2019). Architectonic features and relative locations of primary sensory and related areas of neocortex in mouse lemurs. J. Comp. Neurol 527, 625–639. [PubMed: 29484648]
24. Grinvald A, Frostig RD, Siegel RM, and Bartfeld E (1991). High-resolution optical imaging of functional brain architecture in the awake monkey. Proc. Natl. Acad. Sci. USA 88, 11559–11563. [PubMed: 1763070]
25. Hubel DH, and Wiesel TN (1968). Receptive fields and functional architecture of monkey striate cortex. J. Physiol 195, 215–243. [PubMed: 4966457]
26. Cooper HM, Kennedy H, Magnin M, and Vital-Durand F (1979). Thalamic projections to area 17 in a prosimian primate, Microcebus murinus. J. Comp. Neurol 187, 145–167. [PubMed: 114550]
27. Bonhoeffer T, and Grinvald A (1991). Iso-orientation domains in cat visual cortex are arranged in pinwheel-like patterns. Nature 353, 429–431. [PubMed: 1896085]
28. Schottdorf M, Keil W, Coppola D, White LE, and Wolf F (2015). Random Wiring, Ganglion Cell Mosaics, and the Functional Architecture of the Visual Cortex. PLoS Comput. Biol 11, e1004602. [PubMed: 26575467]
29. Stephan H, Frahm H, and Baron G (1981). New and revised data on volumes of brain structures in insectivores and primates. Folia Primatol. (Basel) 35, 1–29. [PubMed: 7014398]
30. Wolf F (2005). Symmetry, multistability, and long-range interactions in brain development. Phys. Rev. Lett 95, 208701. [PubMed: 16384113]
31. Kaschube M, Schnabel M, Wolf F, and Löwel S (2009). Interareal co-ordination of columnar architectures during visual cortical development. Proc. Natl. Acad. Sci. USA 106, 17205–17210. [PubMed: 19805149]
32. Horton JC, and Adams DL (2005). The cortical column: a structure without a function. Philos. Trans. R. Soc. Lond. B Biol. Sci 360, 837–862. [PubMed: 15937015]
33. Hubel DH, and Wiesel TN (1969). Anatomical demonstration of columns in the monkey striate cortex. Nature 221, 747–750. [PubMed: 4974881]
34. Adams DL, and Horton JC (2003). Capricious expression of cortical columns in the primate brain. Nat. Neurosci 6, 113–114. [PubMed: 12536211]

35. Srinivasan S, Carlo CN, and Stevens CF (2015). Predicting visual acuity from the structure of visual cortex. Proc. Natl. Acad. Sci. USA 112, 7815–7820. [PubMed: 26056277]
36. da Silva Souza G, Gomes BD, and Silveira LCL (2011). Comparative neurophysiology of spatial luminance contrast sensitivity. Psychol. Neurosci 4, 29–48.
37. Yacoub E, Harel N, and Ugurbil K (2008). High-field fMRI unveils orientation columns in humans. Proc. Natl. Acad. Sci. USA 105, 10607–10612. [PubMed: 18641121]
38. Durbin R, and Mitchison G (1990). A dimension reduction framework for understanding cortical maps. Nature 343, 644–647. [PubMed: 2304536]
39. Wolf F, and Geisel T (1998). Spontaneous pinwheel annihilation during visual development. Nature 395, 73–78. [PubMed: 9738500]
40. Keil W, and Wolf F (2011). Coverage, continuity, and visual cortical architecture. Neural Syst. Circuits 1, 17. [PubMed: 22329968]
41. da Costa NM, and Martin KAC (2010). Whose Cortical Column Would that Be? Front. Neuroanat 4, 16. [PubMed: 20640245]
42. Ben-Yishai R, Bar-Or RL, and Sompolinsky H (1995). Theory of orientation tuning in visual cortex. Proc. Natl. Acad. Sci. USA 92, 3844–3848. [PubMed: 7731993]
43. Douglas RJ, Koch C, Mahowald M, Martin KA, and Suarez HH (1995). Recurrent excitation in neocortical circuits. Science 269, 981–985. [PubMed: 7638624]
44. Murphy BK, and Miller KD (2009). Balanced amplification: a new mechanism of selective amplification of neural activity patterns. Neuron 61, 635–648. [PubMed: 19249282]
45. Paradiso MA (1988). A theory for the use of visual orientation information which exploits the columnar structure of striate cortex. Biol. Cybern 58, 35–49. [PubMed: 3345319]
46. Haug H (1987). Brain sizes, surfaces, and neuronal sizes of the cortex cerebri: a stereological investigation of man and his variability and a comparison with some mammals (primates, whales, marsupials, insectivores, and one elephant). Am. J. Anat 180, 126–142. [PubMed: 3673918]
47. Gabi M, Collins CE, Wong P, Torres LB, Kaas JH, and Herculano-Houzel S (2010). Cellular scaling rules for the brains of an extended number of primate species. Brain, Behavior and Evolution 76, 32–44.
48. Herculano-Houzel S, Manger PR, and Kaas JH (2014). Brain scaling in mammalian evolution as a consequence of concerted and mosaic changes in numbers of neurons and average neuronal cell size. Front. Neuroanat 8, 77. [PubMed: 25157220]
49. Kremkow J, Jin J, Wang Y, and Alonso JM (2016). Principles underlying sensory map topography in primary visual cortex. Nature 533, 52–57. [PubMed: 27120164]
50. Lee K-S, Huang X, and Fitzpatrick D (2016). Topology of ON and OFF inputs in visual cortex enables an invariant columnar architecture. Nature 533, 90–94. [PubMed: 27120162]
51. Lien AD, and Scanziani M (2018). Cortical direction selectivity emerges at convergence of thalamic synapses. Nature 558, 80–86. [PubMed: 29795349]
52. Blasdel GG, and Fitzpatrick D (1984). Physiological organization of layer 4 in macaque striate cortex. J. Neurosci 4, 880–895. [PubMed: 6200586]
53. Livingstone M, and Hubel D (1988). Segregation of form, color, movement, and depth: anatomy, physiology, and perception. Science 240, 740–749. [PubMed: 3283936]
54. Jang J, Song M, and Paik S-B (2020). Retino-Cortical Mapping Ratio Predicts Columnar and Salt-and-Pepper Organization in Mammalian Visual Cortex. Cell Rep 30, 3270–3279.e3. [PubMed: 32160536]
55. Dkhissi-Benyahya O, Szel A, Degrip WJ, and Cooper HM (2001). Short and mid-wavelength cone distribution in a nocturnal Strepsirrhine primate (Microcebus murinus). J. Comp. Neurol 438, 490–504. [PubMed: 11559903]
56. Harris KD, and Mrsic-Flogel TD (2013). Cortical connectivity and sensory coding. Nature 503, 51–58. [PubMed: 24201278]
57. Kaas JH (2007). 3.03 - Reconstructing the Organization of Neocortex of the First Mammals and Subsequent Modifications. In Evolution of Nervous Systems, Kaas JH, ed. (Oxford: Academic Press), pp. 27–48.

58. Silcox MT, and López-Torres S (2017). Major Questions in the Study of Primate Origins. Annu. Rev. Earth Planet. Sci 45, 113–137.
59. Bertrand OC, Amador-Mughal F, and Silcox MT (2016). Virtual endo-casts of Eocene Paramys (Paramyinae): oldest endocranial record for Rodentia and early brain evolution in Euarchontoglires. Proc. Biol. Sci 283, 20152316, 10.1098/rspb.2015.2316. [PubMed: 26817776]
60. Li M, Liu F, Jiang H, Lee TS, and Tang S (2017). Long-Term Two-Photon Imaging in Awake Macaque Monkey. Neuron 93, 1049–1057.e3. [PubMed: 28215557]
61. Huebner F, Fichtel C, and Kappeler PM (2018). Linking cognition with fitness in a wild primate: fitness correlates of problem-solving performance and spatial learning ability. Philos. Trans. R. Soc. Lond. B Biol. Sci 373, 20170295, 10.1098/rstb.2017.0295. [PubMed: 30104438]
62. Perret M (2005). Relationship between urinary estrogen levels before conception and sex ratio at birth in a primate, the gray mouse lemur. Hum. Reprod 20, 1504–1510. [PubMed: 15790612]
63. Languille S, Blanc S, Blin O, Canale CI, Dal-Pan A, Devau G, Dhenain M, Dorieux O, Epelbaum J, Gomez D, et al. (2012). The grey mouse lemur: a non-human primate model for ageing studies. Ageing Res. Rev 11, 150–162. [PubMed: 21802530]
64. Jones JPG, Ratsimbazafy J, Ratsifandrihamanana AN, Watson JEM, Andrianandrasana HT, Cabeza M, Cinner JE, Goodman SM, Hawkins F, Mittermeier RA, et al. (2019). Madagascar: Crime threatens biodiversity. Science 363, 825.
65. Schneider CA, Rasband WS, and Eliceiri KW (2012). NIH Image to ImageJ: 25 years of image analysis. Nat. Methods 9, 671–675. [PubMed: 22930834]
66. Mathis A, Mamidanna P, Cury KM, Abe T, Murthy VN, Mathis MW, and Bethge M (2018). DeepLabCut: markerless pose estimation of user-defined body parts with deep learning. Nat. Neurosci 21, 1281–1289. [PubMed: 30127430]
67. Suter BA, O'Connor T, Iyer V, Petreanu LT, Hooks BM, Kiritani T, Svoboda K, and Shepherd GMG (2010). Ephus: multipurpose data acquisition software for neuroscience experiments. Front. Neural Circuits 4, 100. [PubMed: 21960959]
68. Kaschube M, Wolf F, Puhlmann M, Rathjen S, Schmidt K-F, Geisel T, and Löwel S (2003). The pattern of ocular dominance columns in cat primary visual cortex: intra- and interindividual variability of column spacing and its dependence on genetic background. Eur. J. Neurosci 18, 3251–3266. [PubMed: 14686899]
69. Languille S, Aujard F, and Pifferi F (2012). Effect of dietary fish oil supplementation on the exploratory activity, emotional status and spatial memory of the aged mouse lemur, a non-human primate. Behav. Brain Res 235, 280–286. [PubMed: 22921374]
70. Sincich LC, Adams DL, and Horton JC (2003). Complete flatmounting of the macaque cerebral cortex. Vis. Neurosci 20, 663–686. [PubMed: 15088719]
71. Wong-Riley M (1979). Changes in the visual system of monocularly sutured or enucleated cats demonstrable with cytochrome oxidase histochemistry. Brain Res 171, 11–28. [PubMed: 223730]
72. Huber D, Gutnisky DA, Peron S, O'Connor DH, Wiegert JS, Tian L, Oertner TG, Looger LL, and Svoboda K (2012). Multiple dynamic representations in the motor cortex during sensorimotor learning. Nature 484, 473–478. [PubMed: 22538608]
73. Okamoto T, Ikezoe K, Tamura H, Watanabe M, Aihara K, and Fujita I (2011). Predicted contextual modulation varies with distance from pinwheel centers in the orientation preference map. Sci. Rep 1, 114. [PubMed: 22355631]
74. Ratzlaff EH, and Grinvald A (1991). A tandem-lens epifluorescence macroscope: hundred-fold brightness advantage for wide-field imaging. J. Neurosci. Methods 36, 127–137. [PubMed: 1905769]
75. Yokoo T, Knight BW, and Sirovich L (2001). An optimization approach to signal extraction from noisy multivariate data. Neuroimage 14, 1309–1326. [PubMed: 11707087]
76. Fekete T, Omer DB, Naaman S, and Grinvald A (2009). Removal of spatial biological artifacts in functional maps by local similarity minimization. J. Neurosci. Methods 178, 31–39. [PubMed: 19101591]
77. Herculano-Houzel S, Watson C, and Paxinos G (2013). Distribution of neurons in functional areas of the mouse cerebral cortex reveals quantitatively different cortical zones. Front. Neuroanat 7, 35. [PubMed: 24155697]

78. Mengler L, Khmelinskii A, Diedenhofen M, Po C, Staring M, Lelieveldt BPF, and Hoehn M (2014). Brain maturation of the adolescent rat cortex and striatum: changes in volume and myelination. Neuroimage 84, 35–44. [PubMed: 23994458]

79. Krubitzer L, Campi KL, and Cooke DF (2011). All rodents are not the same: a modern synthesis of cortical organization. Brain, Behavior and Evolution 78, 51–93.

80. Keeley RJ, Burger DK, Saucier DM, and Iwaniuk AN (2015). The size of non-hippocampal brain regions varies by season and sex in Richardson's ground squirrel. Neuroscience 289, 194–206. [PubMed: 25595988]

81. Santiago LF, Freire MAM, Picanço-Diniz CW, Franca JG, and Pereira A (2019). The Organization and Connections of Second Somatosensory Cortex in the Agouti. Front. Neuroanat 12, 118. [PubMed: 30692919]

82. Campos GB, and Welker WI (1976). Comparisons between brains of a large and a small hystricomorph rodent: capybara, Hydrochoerus and guinea pig, Cavia; neocortical projection regions and measurements of brain subdivisions. Brain Behav. Evol 13, 243–266. [PubMed: 990909]

83. Lewitus E, Hof PR, and Sherwood CC (2012). Phylogenetic comparison of neuron and glia densities in the primary visual cortex and hippo-campus of carnivores and primates. Evolution 66, 2551–2563. [PubMed: 22834752]

84. Rockel AJ, Hiorns RW, and Powell TP (1980). The basic uniformity in structure of the neocortex. Brain 103, 221–244. [PubMed: 6772266]

85. McLoughlin N, and Schiessl I (2006). Orientation selectivity in the common marmoset (Callithrix jacchus): the periodicity of orientation columns in V1 and V2. Neuroimage 31, 76–85. [PubMed: 16487727]

Highlights

- Mouse lemur V1 possesses orientation preference maps with pinwheel arrangement
- The size and statistics of mouse lemur V1 pinwheels are comparable to the macaque
- Orientation preference columns only weakly scale with body size in primates

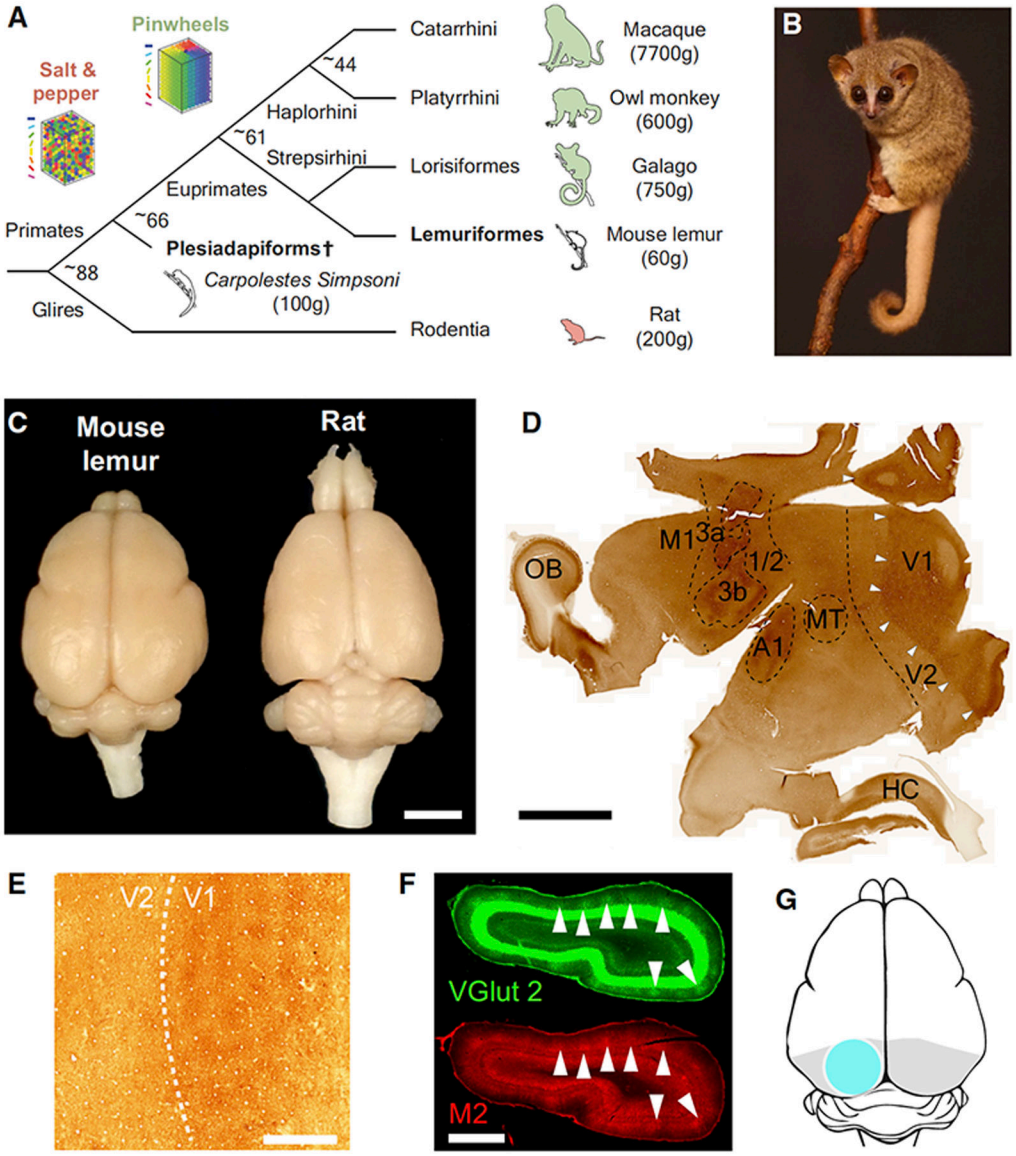

Figure 1. Mouse Lemur (*Microcebus murinus*)

(A) Schematic tree of rodent and primate evolution. Species where V1 pinwheels have been reported are labeled in green; species with salt and pepper organization are in red. Numbers at the bifurcation points are approximative ages in millions of years (from Seiffert et al.;[17] however, see also O'Leary et al. and Zhang et al.[2,18] Primate-glire split date taken from Huchon et al.[19]).

(B) A mouse lemur climbing on a branch.

(C) Size comparison of a mouse lemur brain (left) and a rat brain (right; scale bar, 5 mm).

(D) Cytochrome oxidase (CO) staining of a flat-mounted mouse lemur cortex. The visual cortex is clearly delineated (white arrows) by the dark and patchy appearance of the CO staining. OB: olfactory bulb; M1: primary motor cortex; 3a, 3b, 1/2: areas of the primary somatosensory cortex; A1: auditory cortex; MT: medial temporal cortex; V1, V2: primary secondary visual cortex; HC: hippocampus. Scale bar, 5 mm.

(E) High-resolution view of a CO staining in a flat mount with a patch-like pattern in the V1. Scale bar, 1 mm.

(F) Two adjacent coronal sections through V1 with immunolabeling for vesicular glutamate transporter 2 (VGlut2) and the muscarinic receptor 2 (M2). The arrows indicate overlapping patches of dense fiber labeling in supra-granular layers. Representative example for n = 2 animals. Scale bar, 1 mm.

(G) Schematic top view of the mouse lemur brain with V1 outlined in gray and the location of the chronic imaging window in light blue.

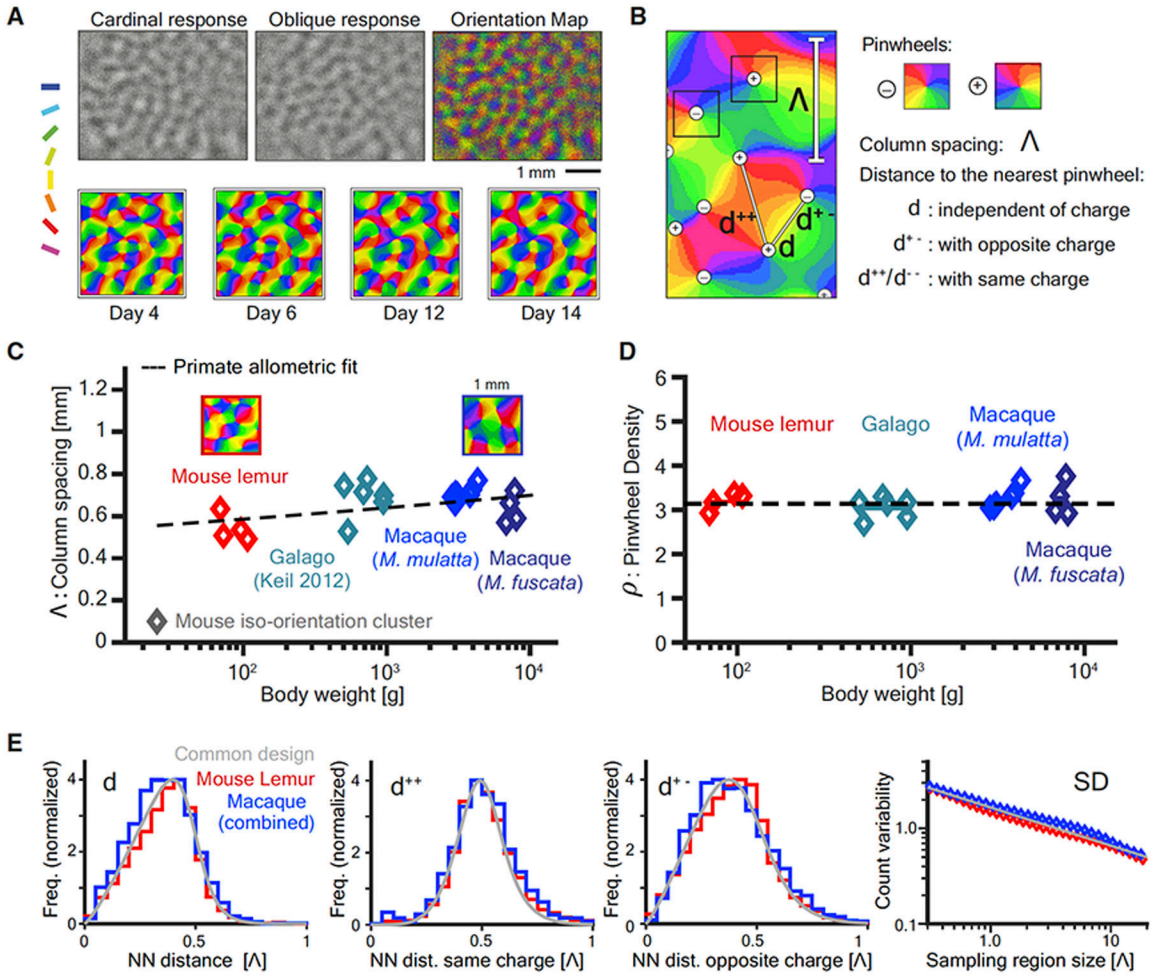

Figure 2. Orientation Preference Maps and Map Statistics

(A) Intrinsic signal imaging responses obtained by subtracting responses to the two cardinal and two oblique directions, respectively, displayed as a color-coded orientation map. The responses were stable for up to 14 days of chronic imaging (bottom row; see also Figure S1).

(B) Graphical depiction of the definitions of column spacing and pinwheel distances. Pinwheels can assume one of two discrete "charges" —positive or negative—depending on the topological arrangement of orientation preference around the pinwheel center. The nearest neighbor (NN) distance is the shortest distance between pinwheels, dependent or independent of charge.

(C) Column spacing of the mouse lemur and macaques (*Macaca fuscata* and *Macaca mulatta*) among the primates (adapted from Keil et al.[14]). Primate allometric fit to species means to guide the eye: $y = 0.4903 \times^{0.03842}$ (See also Figure S2A).

(D) Pinwheel density of the mouse lemur and macaque among the primates (data from Schottdorf et al.,'[28] symbol size proportional to the area of measured region in units of Λ^2; see also Figure S2B).

(E) Characteristics of the mouse lemur pinwheels (red) in comparison with the macaque (both species pooled) and the common design model[13] (gray).

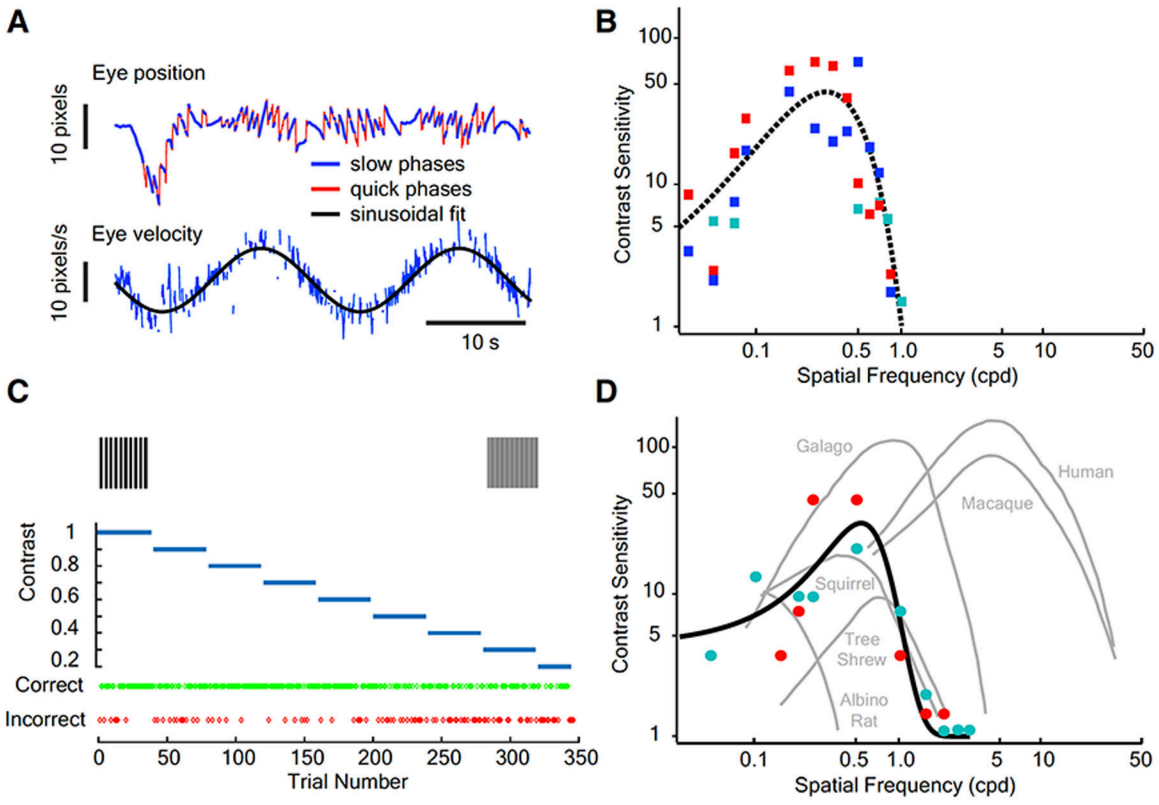

Figure 3. Visual Acuity of the Mouse Lemur

(A) Visual reflex threshold estimation using the optokinetic reflex (OKR) response. Example data from eye movements evoked by two 0.05-Hz rotation cycles of a virtual drum consisting of vertical black and white stripes (spatial frequency = 0.1678 and contrast = 1). The velocity trace of the OKR slow phases was fit with a 0.05-Hz sinusoidal function.

(B) Averaged contrast sensitivity threshold (dotted line) based on the OKR of three animals (colored points).

(C) Example session with the behavioral performance of an animal (red points in B and D) at 1.5 cpd and various contrasts. Gratings in the inset are not drawn to scale (see also Video S1).

(D) Contrast sensitivity curve was fitted to the combined and averaged behavioral contrast sensitivity thresholds of two mouse lemurs. The colors of the individual animals correspond to the same identity as in (B).

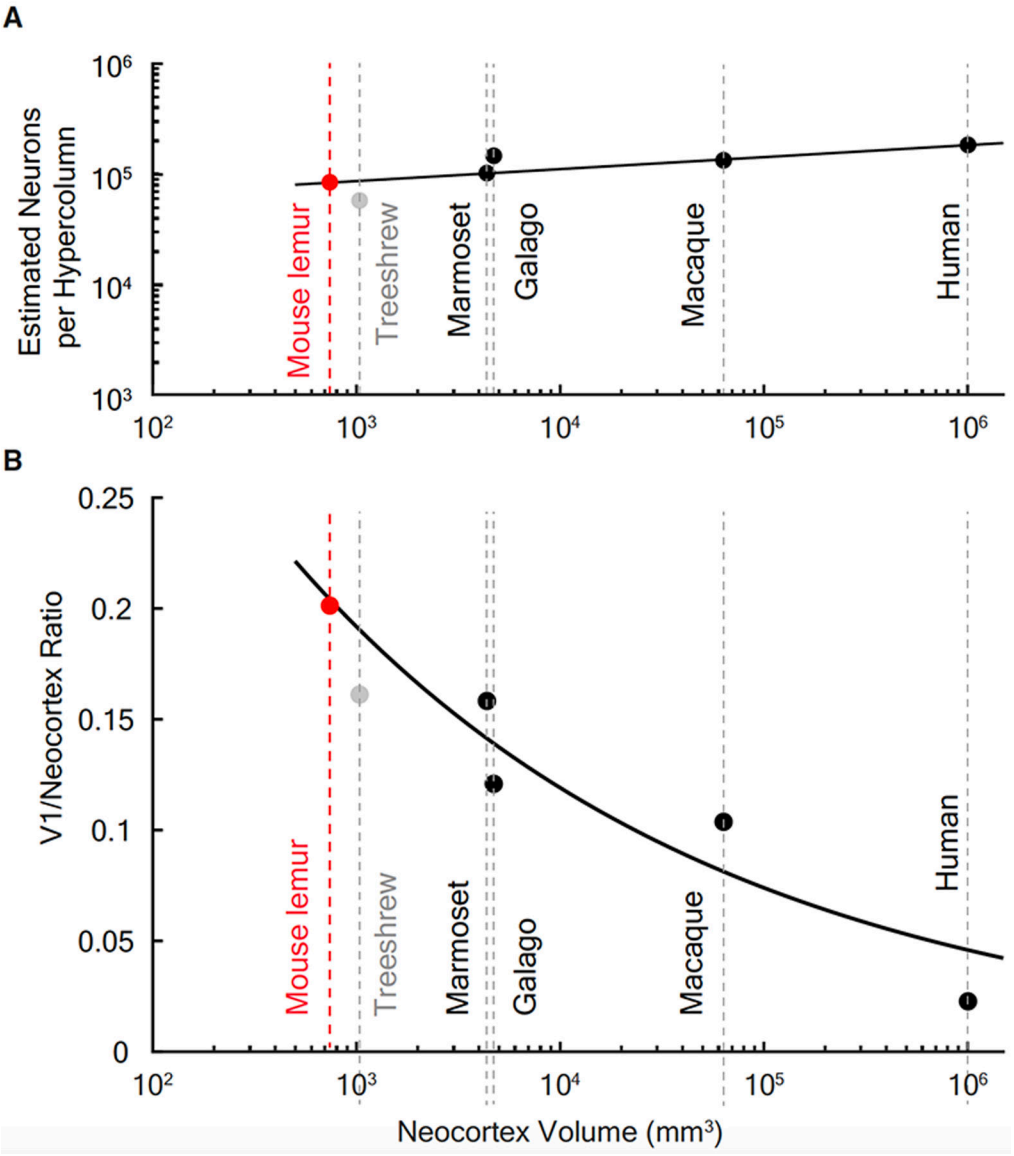

Figure 4. Estimated Neurons per Hypercolumn and V1-to-Neocortex Ratio

(A) Estimated number of neurons per hypercolumn for the mouse lemur in relation to other primates and the tree shrew (see STAR Methods for details and references). Fitted line $y = 4.1*10^4 \times^{0.1081}$.

(B) V1-to-cortex ratio of primates (fitted line $y = 0.801x^{-0.2069}$) and tree shrew for comparison (see also Figure S4).

KEY RESOURCES TABLE

REAGENT or RESOURCE	SOURCE	IDENTIFIER
Antibodies		
Guinea pig Anti-VGLUT2, Unconjugated antibody	Millipore	Cat# AB2251; RRID:AB_1587626
Anti-Muscarinic Acetylcholine Receptor m2, clone M2-2-B3 antibody	Millipore	Cat# MAB367; RRID:AB_94952
Rabbit Anti-VGIuT2, polyclonal	Synaptic Systems	SySyl 35403; RRID:AB_887883
Chemicals, Peptides, and Recombinant Proteins		
Cytochrome c from equine heart	Sigma Aldrich	C2506 CAS# 9007-43-6
3,3 ¢-Diaminobenzidine	Sigma Aldrich	D4293 MDL# MFCD00007725
Experimental Models: Organisms/Strains		
Microcebus murinus	https://micmu.cnrs.fr/	NCBI:txid30608
Macaca fuscata		NCBI:txid9542
Macaca mulatta		NCBI:txid9544
Software and Algorithms		
ImageJ	Schneider et al.[65]	https://imagej.nih.gov/ij/
MATLAB	MathWorks	MATLAB 2003; 2015
DeepLabCut	Mathis et al.[66]	https://github.com/DeepLabCut/DeepLabCut
Ephus	Suter et al.[67]	scanimage.org
Code for column spacing estimation	Kaschube et al.[68]	N/A
Code for pinwheel statistics analysis	Schottdorf et al[28]	N/A
Code for mouse lemur visual acuity	This paper	https://doi:10.26037/yareta:n2u7jm3wf5he7p6xpecta4gktm